Development of activity pencil beam algorithm using measured distribution data of positron emitter nuclei generated by proton irradiation of targets containing ^{12}C, ^{16}O, and ^{40}Ca nuclei in preparation of clinical application

Aya Miyatake[a]
Keen Medical Physics Services, 2-11-8 yayoi, Bunkyo-ku, Tokyo 113-0032, Japan

Teiji Nishio and Takashi Ogino
Particle Therapy Division, Research Center for Innovative Oncology, National Cancer Center, Kashiwa, 6-5-1 Kashiwano-ha, Kashiwa-shi, Chiba 277-8577, Japan

Purpose: The purpose of this study is to develop a new calculation algorithm that is satisfactory in terms of the requirements for both accuracy and calculation time for a simulation of imaging of the proton-irradiated volume in a patient body in clinical proton therapy.

Methods: The activity pencil beam algorithm (APB algorithm), which is a new technique to apply the pencil beam algorithm generally used for proton dose calculations in proton therapy to the calculation of activity distributions, was developed as a calculation algorithm of the activity distributions formed by positron emitter nuclei generated from target nuclear fragment reactions. In the APB algorithm, activity distributions are calculated using an activity pencil beam kernel. In addition, the activity pencil beam kernel is constructed using measured activity distributions in the depth direction and calculations in the lateral direction. ^{12}C, ^{16}O, and ^{40}Ca nuclei were determined as the major target nuclei that constitute a human body that are of relevance for calculation of activity distributions. In this study, "virtual positron emitter nuclei" was defined as the integral yield of various positron emitter nuclei generated from each target nucleus by target nuclear fragment reactions with irradiated proton beam. Compounds, namely, polyethylene, water (including some gelatin) and calcium oxide, which contain plenty of the target nuclei, were irradiated using a proton beam. In addition, depth activity distributions of virtual positron emitter nuclei generated in each compound from target nuclear fragment reactions were measured using a beam ON-LINE PET system mounted a rotating gantry port (BOLPs-RGp). The measured activity distributions depend on depth or, in other words, energy. The irradiated proton beam energies were 138, 179, and 223 MeV, and measurement time was about 5 h until the measured activity reached the background level. Furthermore, the activity pencil beam data were made using the activity pencil beam kernel, which was composed of the measured depth data and the lateral data including multiple Coulomb scattering approximated by the Gaussian function, and were used for calculating activity distributions.

Results: The data of measured depth activity distributions for every target nucleus by proton beam energy were obtained using BOLPs-RGp. The form of the depth activity distribution was verified, and the data were made in consideration of the time-dependent change of the form. Time dependence of an activity distribution form could be represented by two half-lives. Gaussian form of the lateral distribution of the activity pencil beam kernel was decided by the effect of multiple Coulomb scattering. Thus, the data of activity pencil beam involving time dependence could be obtained in this study.

Conclusions: The simulation of imaging of the proton-irradiated volume in a patient body using target nuclear fragment reactions was feasible with the developed APB algorithm taking time dependence into account. With the use of the APB algorithm, it was suggested that a system of simulation of activity distributions that has levels of both accuracy and calculation time appropriate for clinical use can be constructed. © *2011 American Association of Physicists in Medicine.*
[DOI: 10.1118/1.3641829]

Key words: proton therapy, proton beam monitoring, simulation of activity distribution, activity pencil beam algorithm, beam ON-LINE PET system, target nuclear fragment reaction

I. INTRODUCTION

The Beam ON-LINE PET system mounted on a rotating gantry port (BOLPs-RGp) was previously developed, and proton therapy has been performed for all patients with measurement using BOLPs-RGp at the National Cancer Center, Kashiwa, since October, 2007.[1] This system measures annihilation gamma rays generated from the irradiated volume in

a patient body from the start of proton beam irradiation to 200 s after the end of irradiation using BOLPs-RGp. Up to now, the number of cases measured is about 150, such as cases involving head and neck, prostate, liver, lung, and brain. Furthermore, an apparatus for viewing and analysis, which exclusively uses the data measured by BOLPs-RGp, has been developed and used.[2] Study involving analysis of irradiated body tissues of patients using clinical data has been reported,[1,2] which proved that the use of BOLPs-RGp in clinical proton therapy is very useful for quality assurance and control and provides improvement in terms of accuracy.

Research in the monitoring of the proton-irradiated volume via nucleus activation has been worked on.[1–17] To verify the absolute accuracy of planned dose distributions using measured activity distributions, we have to simulate activity distributions from dose distributions. Research on the simulation of activity distributions has been carried out. One of the methods is calculation of activity distributions using a Monte Carlo simulation, in which data of cross sections for the rate of target nuclear fragment reactions between proton and nuclei compositing patients' bodies are used with GEANT4 and FLUKA.[18–20] And, in carbon ion therapy it is reported that a technique of activity simulation utilizes the database of Monte Carlo calculated activity distribution which is formed in ^{12}C pencil beam irradiation of PMMA targets.[21] That research group deals with both projectile and target nuclear fragmentation reactions but only target nuclear fragments are treated in this study. It is difficult to determine the value of cross sections as the value is dependent on proton energy and the species of positron emitter nuclei that are generated. At present, the reported data of cross sections are not sufficient for simulation of activity distributions in terms of quantity and accuracy.[22] However, determination of the value of cross sections is now underway in other groups, and it may be expected that data of cross sections that are sufficient for simulation will be obtained. Therefore, it can be said that the calculation accuracy of simulation based on a detailed physics process using a Monte Carlo simulation will likely improve with a corresponding increased accuracy in the knowledge of reaction cross sections in the near future.

To use the simulation in clinical therapy, the calculation time is one of the necessary conditions in addition to the calculation accuracy. Because an enormous amount of data is essential for calculation using the Monte Carlo simulation, which is a statistical calculation method with random numbers, it takes hours to obtain the result of calculation. Although there are methods, like lookup table, e.g., phase-space file, to improve the speed of simulation such as GEANT and FLUKA, it may be difficult to adopt the simulation system using the Monte Carlo simulation for an on-site location near a clinical therapy where it is now needed for treatment of a lot of patients. However, since BOLPs-RGp is now used in clinical therapy, there are ongoing efforts of constructing a simulation system that meets the requirements in terms of both accuracy and calculation time for clinical use. It is necessary to develop a new calculation algorithm that can be used in clinical therapy to provide improvements in proton therapy using BOLPs-RGp.

The purpose of this study is to develop a new calculation algorithm for the simulation system of imaging of activity distributions corresponding to the planned irradiation volume in clinical proton therapy.
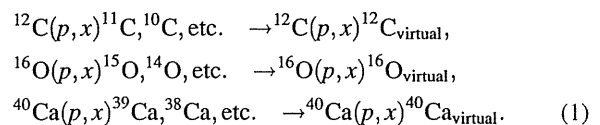
II. MATERIAL AND METHOD

II.A. The new calculation algorithm of activity distributions proposed in this study

The necessary conditions of the calculation algorithm of activity distributions are high speed and high accuracy in calculation for utilization of the simulation system for imaging of activity distributions in clinical proton therapy. The new algorithm was developed using activity pencil beam kernel for calculation of activity distributions in this study. The data of measured depth activity distributions and calculated lateral activity distributions are used for obtaining the activity pencil beam data.

II.A.1. Depth activity distribution

A quantity of positron emitter nuclei generated from target nuclear fragment reactions is affected by each value of the cross section for the reactions within the range of energy used for proton therapy. Since the accuracy of the value regarding the cross section has a direct effect on the accuracy of the simulation, the determined value for the cross section is very important in the simulation of activity distributions. However, it cannot be said that the data of the cross section required for simulation calculation are sufficient in terms of accuracy and quantity at present. The phantom study using PET/CT imaging suggested the potential of millimeter accuracy in proton therapy.[16] But in patient study, it was reported that the accuracy of a simulation that calculated activity distributions in a patient body was within 30% by uncertainties of cross section, washout effects, and stoichiometric composition in patient body.[15]

Therefore, improvements in the accuracy of values regarding the cross sections of target nuclear fragment reactions are needed to use the simulation of activity distributions to image the planned and proton-irradiated volume with high accuracy in clinical proton therapy. In this study, "virtual positron emitter nuclei (^{12}C$_{virtual}$, ^{16}O$_{virtual}$, and ^{40}Ca$_{virtual}$)" was defined as the nuclei merged of various positron emitter nuclei generated from each target nucleus by target nuclear fragment reactions with irradiated proton beam (see Eq. (1)).

$$^{12}C(p,x)^{11}C, ^{10}C, \text{etc.} \rightarrow ^{12}C(p,x)^{12}C_{virtual},$$
$$^{16}O(p,x)^{15}O, ^{14}O, \text{etc.} \rightarrow ^{16}O(p,x)^{16}O_{virtual},$$
$$^{40}Ca(p,x)^{39}Ca, ^{38}Ca, \text{etc.} \rightarrow ^{40}Ca(p,x)^{40}Ca_{virtual}. \quad (1)$$

A new approach was adopted that uses measured activity distributions of virtual positron emitter nuclei when the proton beam irradiates a compound containing target nuclei, not which uses values of reaction cross section determined one by one for each reaction channel. The data of measured activity distributions of virtual positron emitter nuclei that we obtained

in this study cover the information of the most relevant reaction channels generating positron emitter nuclei in irradiation targets. Moreover, decrease of energy and attenuation of incident proton flux occur at the depth point in thick targets. A similar attenuate phenomenon occurs in a patient body irradiated by proton beam. Therefore, the data are significant for this study in view of future application to describe the nuclear fragmentation reactions occurring in the human body. In the calculation of activity distributions, measured data of depth activity distributions can improve the accuracy of calculation.

II.A.2. Calculation algorithm of activity distributions for simulation of imaging of planned irradiation volume by proton beam: activity pencil beam algorithm (APB algorithm)

The accuracy of calculation using the Monte Carlo simulation is affected by statistical error, which depends on the total number of histories. Calculation must be performed with a sufficiently large number of histories to meet the accuracy required in each case. With the Monte Carlo simulation, it takes hours to obtain the result of calculation with the accuracy required for clinical use. A simulation with calculation time within several minutes is demanded for proton therapy of many patients in hospital.

For simulation system of imaging of activity distributions in daily proton therapy, the activity pencil beam algorithm (APB algorithm) was developed as a new calculation algorithm with both accuracy and high speed. The pencil beam algorithm is a standard algorithm of dose calculation in proton therapy. This algorithm is a technique for calculation that considers depth dose distributions along the direction that the proton beam travels, and that also approximates lateral dose distributions of the Gaussian form at every depth point by effect of multiple Coulomb scattering. However, effect of the scattering by inhomogeneous density in material from axis of beam direction is not considered in the pencil beam algorithm. Therefore, the accuracy of calculation of dose distributions deteriorates in areas of a steep density gradient, such as lungs, bone, and nasal cavity. Although the accuracy of calculation using pencil beam algorithm may deteriorate in a site of a patient's body, the algorithm is generally used for dose calculation in clinical proton therapy because it is well balanced between accuracy and calculation time required in clinical use. These considerations are similar in APB algorithm for the calculation of activity distributions formed by target nuclear fragment reactions between proton and nuclei compositing a human body.

In APB algorithm, depth and lateral activity distributions are defined by measurement of activity of ^{12}C$_{virtual}$, ^{16}O$_{virtual}$ and ^{40}Ca$_{virtual}$ nuclei and calculation of multiple Coulomb scattering. The activity pencil beam kernel, $A_{mono}(X_{virtual}; r, z, t_{ag})$, is shown in Eq. (2) as following:

$$A_{mono}\left(X_{virtual}; r, z, t_{ag}\right) = A_{meas.}\left(X_{virtual}; z, t_{ag}\right) \cdot \frac{1}{2 \cdot \pi \cdot \sigma_r(z)^2}$$
$$\cdot \exp\left(-\frac{r^2}{2 \cdot \sigma_r(z)^2}\right),$$
$$\{X_{virtual} = {}^{12}C_{virtual}, {}^{16}O_{virtual}, {}^{40}Ca_{virtual}\}. \tag{2}$$

Here, $A_{meas.}\left(X_{virtual}; r, z, t_{ag}\right)$ is measured depth activity distribution, $X_{virtual}$ virtual positron emitter nuclei, r lateral position from axis of beam direction, z depth point in water equivalent material, t_{ag} time after generated virtual positron emitter nuclei, and σ_r the parameter of lateral distribution decided by effect of multiple Coulomb scattering. There are various techniques to decide parameter of σ_r.[23-26] If APB algorithm is adopted, it can be estimated that the calculation time will be several minutes because activity calculation time is similar to dose calculation time using pencil beam algorithm theoretically. Therefore, the calculation time required in clinical use will be satisfied.

II.B. Beam ON-LINE PET system mounted on a rotating gantry port: BOLPs-RGp

The beam ON-LINE PET system mounted on a rotating gantry port (BOLPs-RGp) installed on the proton beam line in our treatment room in the National Cancer Center, Kashiwa, was developed for proton beam monitoring and is used in clinical proton therapy.[1] The opposing detector heads of planar type with a high position resolution were composed of BGO crystals with a crystal size of $2 \times 2 \times 20$ mm^3. The field of view (FOV) at the iso-center was 164.8×167.0 mm^2. The center of its detection area corresponded with the iso-center under a condition where the detectors were opposite each other on a rotating gantry port. The opposing detectors rotated together with the rotating gantry. The detector heads opposite each other were installed along the axis of the proton beam direction and an area in the range direction of the proton beam can be observed. A PET image is reconstructed using a maximum likelihood algorithm taking into consideration the attenuation coefficient of 511-keV gamma rays in the patient's body calculated using the patient's planning CT image data. The distance between the opposing detector heads can be adjusted from 30 to 100 cm.

With regard to the performance of this detection system, the maximum collection rate of the data for the coincident detection was about 1 Mcps. The position resolution of measuring activity was about 2 mm of the full width at half maximum (FWHM) at the iso-center in the FOV in an experiment using a ^{22}Na point source. The detection efficiency was calibrated using a thin-flat acrylic container filled with ^{18}F solution at each distance between detector heads from 30 to 100 cm. In addition, the viewer of activity for clinical analysis (VACA; TR Japan), which is a display and analysis tool for the data detected by BOLPs-RGp, was developed and used.[2]

II.C. Measurement of depth activity distributions

II.C.1. Irradiation target for measurements of activity

The main nuclei of which human body tissue is composed and which cause target nuclear fragment reactions with proton are the following: ^{12}C, ^{14}N, ^{16}O and ^{40}Ca, in the range of proton beam energy used in proton therapy (i.e., 0–250 MeV). Important nuclei for imaging of irradiated volume in a patient's body are ^{12}C, ^{16}O, and ^{40}Ca nuclei by the ratio of

the four nuclei in a human body tissue and the data of a reaction cross section for target nuclear fragment reactions in the range of proton beam energy used in proton therapy.[2] Therefore, ^{12}C nuclei and [16]O nuclei, as well as [40]Ca nuclei, were selected as the target nuclei, and activity distributions of virtual positron emitter nuclear formed from a reaction between proton and the target nuclei were obtained.

Polyethylene (PE: CH_2) and water were the irradiated targets, and activity distributions that originated from a reaction between proton and ^{12}C nuclei or [16]O nuclei were measured. In the experiment using the two targets of PE and water, hydrogen nuclei have no part in the target nuclear fragment reactions. Consequently, the results of measurement for the two targets are equal to the results of reaction for ^{12}C nuclei and [16]O nuclei with proton. The target of PE was made of polyethylene with a high density of 0.96 g/cm^{3}. By addition of a little gelatin (the mass of the gelatin was 1.95% the mass of water) to pure water, a target of water with no flow was made. Because handling of solid calcium is difficult, packed powder of calcium oxide (CaO), which can be handled comparatively easily in a container made of PE, was the target of [40]Ca nuclei. The results of measurement of CaO target included the reaction of proton and [40]Ca nuclei as well as [16]O nuclei. Then, results of only the reaction of [40]Ca nuclei and proton were obtained by subtracting the results of reaction of [16]O nuclei and proton from the results of CaO target. The difference of proton fluence calculated in CaO target and water target was about 5% around range point of 223 MeV proton beam. Result of activity distribution of [40]Ca$_{virtual}$ nuclei was considered by the difference of proton flux attenuation in CaO and water targets.

Considering the detecting area of BOLPs-RGp and the size of the proton beam, the size of PE target was $8 \times 8 \times 12$ cm[3]. Targets of water and CaO were the containers made of PE with a thickness of 5 mm, filled with the water including a little gelatin or the powdered CaO, and the inside volume of the containers was $8 \times 8 \times 12$ cm[3] (see Fig. 1). To acquire the depth activity distributions produced by [40]Ca nuclei and proton nuclei, the number of irradiated proton to target was normalized using activity value of 5-mm thickness wall on the side of the beam entrance in container of PE for water (H_2O) and CaO targets. In experiment of range measurement after passing through the target by the proton beam, the

water equivalent length of 1 cm PE and CaO were 1.02 cm and 1.15 cm, respectively.

II.C.2. Proton beam irradiations to target

Each target was irradiated using mono-energetic proton beams with energies of 223, 179, and 138 MeV. The irradiated dose was equivalent to 15 Gy at around the Bragg Peak to reduce the statistical error of measurement activity of virtual positron emitter nuclei in irradiation target. The proton beam of 2 cm in diameter at the iso-center was irradiated in 2–20 s. Each target was measured on the condition that intensity of proton beams in each measurement and irradiation time in the same energy was constant.

[40]Ca$_{virtual}$ nuclei include positron emitter nuclei with short half-lives around 1 s, such as [38]Ca nuclei and [39]Ca nuclei. Therefore, an additional measurement such that the time of proton beam irradiated to CaO target was less than 1 s was done. The activity measurement was performed twice for each proton beam energy in order to measure the generated positron emitter nuclei of short half-lives with improved statistics.

II.C.3. Measurement of depth activity distributions using BOLPs-RGp

The depth activity distribution of virtual positron emitter nuclei generated by proton beam irradiation in a target was measured using BOLPs-RGp. The irradiation target was set up at the position where the center of the target corresponded to the iso-center (see left side of Fig. 2). The distance between the opposing detector heads of PET was 90 cm and the gantry angle was 270°. The measurement time was 303.3 min (5 h 3 min and 20 s) in one irradiation for each target for obtaining enough characteristic of virtual positron emitter nuclei generated by proton beam irradiation. The output of measurement values occurred every second from the start of measurement to 200 s and, after 200 s, an integrated count for every 10 s was output. For the CaO target, an additional measurement of 200 s was performed. The output of measurement values occurred every second for measurement of virtual positron emitter nuclei with short half-lives generated by proton irradiation.

The FOV of BOLPs-RGp was about 16 cm; however, the proton beam range in water was about 14–30 cm at 138–223 MeV. The area was so small that measurement could not be finished in a single session. Therefore, the whole measurement area of the target was divided in the depth direction, and each separate measurement area was measured gradually. The measurement area was shown in right side of Fig. 2. The numbers of separate areas were five at 223 MeV, three at 179 MeV, and two at 138 MeV. The depicted proton dose distributions were measured using water phantom. The depth of the dose distribution shows water equivalent length (WEL). The method of gradual measurement involved the measurement area being moved by changing the thickness of a fine degrader, which adjusted the beam range, and inserting the PE material with homogeneous thickness into the place at which the patient's bolus was put. Measured depth activity
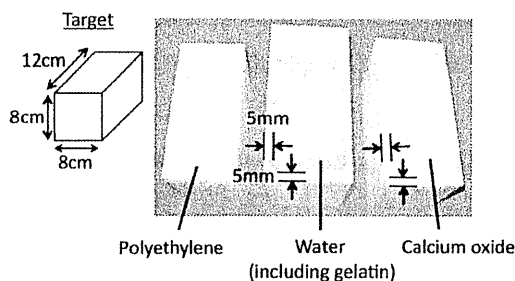

FIG. 1. Targets consisted of the target nuclei, that is, ^{12}C, ^{16}O, and [40]Ca. The left is polyethylene, the middle is water including gelatin, and the right is calcium oxide.

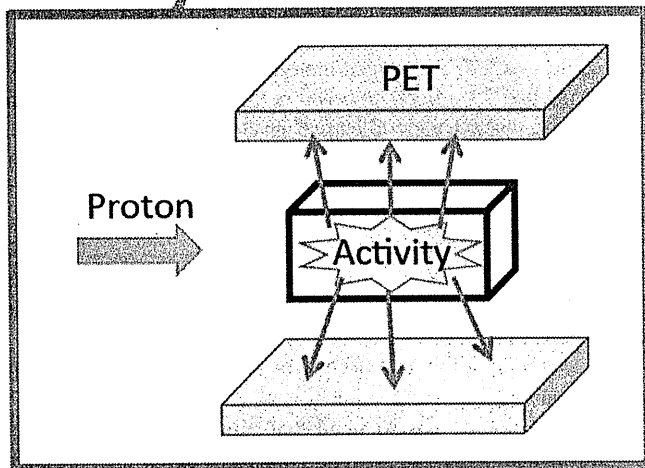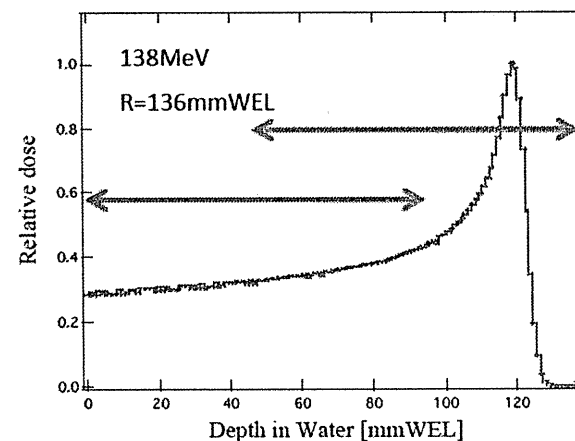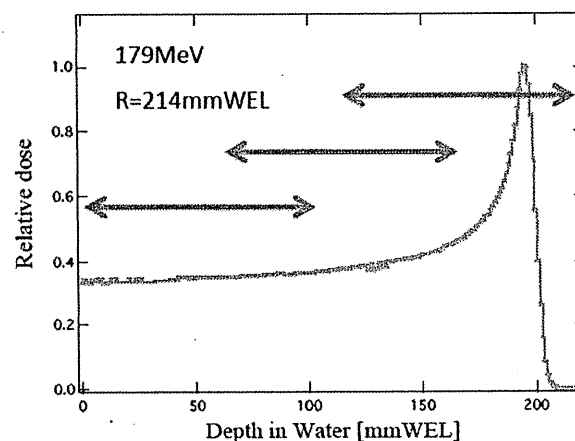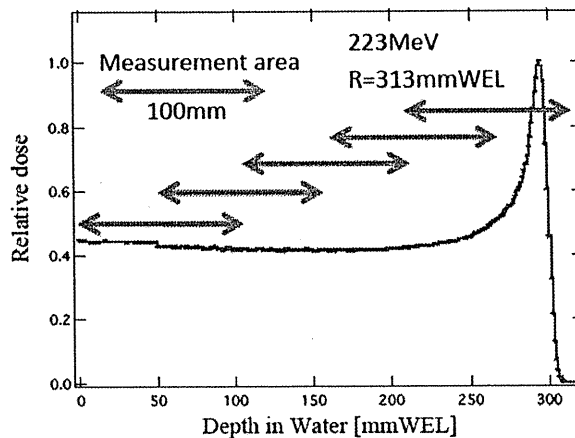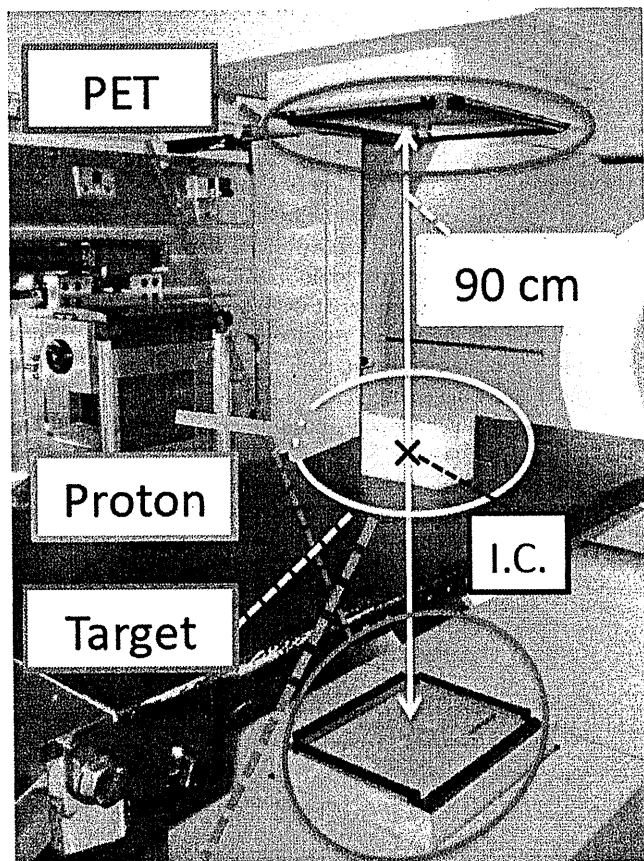Fig. 2. The design of a system to measure activity distributions (left) and measurement area of the target each energy (right) using BOLPs-RGp in NCC, Kashiwa.

distributions for every energy and target were acquired by connecting each measured activity distribution gradually.

II.D. Making of activity pencil beam kernel using the measured activity distributions

The pencil beam algorithm takes into consideration both depth activity distributions along the direction toward the center axis of proton beam travel and lateral activity distri-

bution at depth by effect of multiple Coulomb scattering. In the direction of the center axis of the proton beam, water length equivalent to the length of each calculation grid was calculated, and this calculated length was given a one-dimensional value of percent depth activity (PDA). The effect of multiple Coulomb scattering was included to lateral activity distribution with Gaussian form similarly to proton dose calculation by pencil beam algorithm. The formula
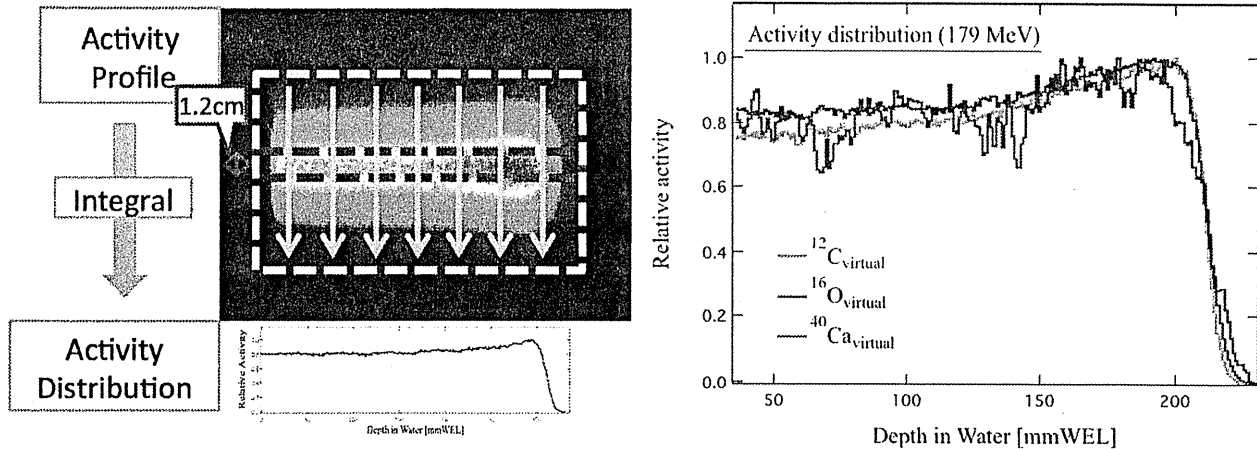
FIG. 3. The approach for making activity distributions from integrated measured two-dimensional activity profile (left). The measured depth activity distributions of virtual positron emitter nuclei that were obtained by irradiating proton beam of 179 MeV to every target nucleus (right).

proposed by Lynch was used for the activity pencil beam kernel in this study.[25]

III. RESULTS AND DISCUSSION

III.A. Results of measured depth activity distributions

The profile of a target activity obtained using BOLPs-RGp is two-dimensional information, which is taken in two perpendicular directions to the opposing detectors of PET installed on BOLPs-RGp. As shown to the left of Fig. 3, first, the measured two-dimensional activity profile was integrated in the direction perpendicular to the beam axis. Second, divided measured data were revised, such as by normalizing the number of incident proton, and the revised data were gathered and connected. This was the case for the results of measured depth activity distributions for every energy and target. Figure 3 shows the measured depth activity distributions obtained by irradiating proton beam of 179 MeV for every target nucleus. In terms of the distribution of $^{40}Ca_{virtual}$ nuclei, it can be seen that the dispersion of $^{40}Ca_{virtual}$ nuclei distribution is greater than that of the other two nuclei. This can be explained by there being statistical dispersion in $^{40}Ca_{virtual}$ nuclei data because $^{40}Ca_{virtual}$ nuclei data are obtained by subtracting $^{16}O_{virtual}$ nuclei data from the CaO data. The dispersion could be reduced by increasing the measurement time and the number of measurement data.

III.B. Verification of the form and the time dependence of depth activity distributions

III.B.1. Depth activity distributions by starting time of measurement after proton beam irradiation

Activity distribution is based on the information of virtual positron emitter nuclei generated by target nuclear fragment reactions. The quantity of activity detected by BOLPs-RGp is dependent on the time of irradiation and detection because positron emitter nuclei have half-lives that differ for every kind of nucleus. Therefore, it is necessary to verify the time dependence of the form of a measured activity distribution during the measurement period. The irradiation time of a

proton beam varies for each patient and treatment by the difference of fractional dose or whether irradiation with synchronized respiration was carried out. Change of depth activity distribution by period of proton irradiation was verified and estimated by the measured activity data using BOLPs-RGp in clinical treatment.[1,2]

About five areas of depth activity distributions of $^{12}C_{virtual}$ nuclei obtained using a proton beam of 223 MeV irradiating PE targets were verified. Figure 4 is measurement results of depth activity distributions by starting time of measurement after 223 MeV proton beam irradiation to PE target. Two activity distributions ((a) and (b)) shown in the figure are measured in the area around entrance of PE target with incident proton beam and the proton beam range of 223 MeV. The measured depth activity distribution data of 100 s was analyzed by the time from irradiation to starting BOLPs-RGp measurement, Ts, of 0 (immediately after the irradiation), 0.5, 1, 2, 3, 5, 7, and 10 min. In the area around entrance of PE target with incident proton beam of 223 MeV, the change of the form of depth activity distributions to the change of Ts was within $\pm 10\%$ [Fig. 4(a)]. In the deepest area around the beam range, although the forms of six depth activity distributions with Ts greater than 1 min were similar, the forms of distributions about $Ts =$ and 0.5 were greatly different from others [Fig. 4(b)]. In these circumstances, it was clear that the form of depth activity distributions changed with the depth and the irradiation time.

Depth activity distributions of $^{12}C_{virtual}$ nuclei obtained by proton beam irradiation to PE are the function of the time and the depth, which were expressed by two elements: ^{10}C nucleus whose half-life is about 20 s and ^{11}C nucleus whose half-life is about 20 min. ^{10}C nuclei with a short half-life are included in activity data measured immediately after proton beam irradiation. As time passed, a difference in the form of the depth activity distribution occurred because mainly information on ^{11}C nuclei became available. Therefore, it can be considered that the reason why the form of the depth activity distribution changed is that the ratio of the amount of information about ^{10}C nuclei and ^{11}C nuclei in the measured data changed with time from the end of irradiation to the start of the measurement (i.e., Ts).
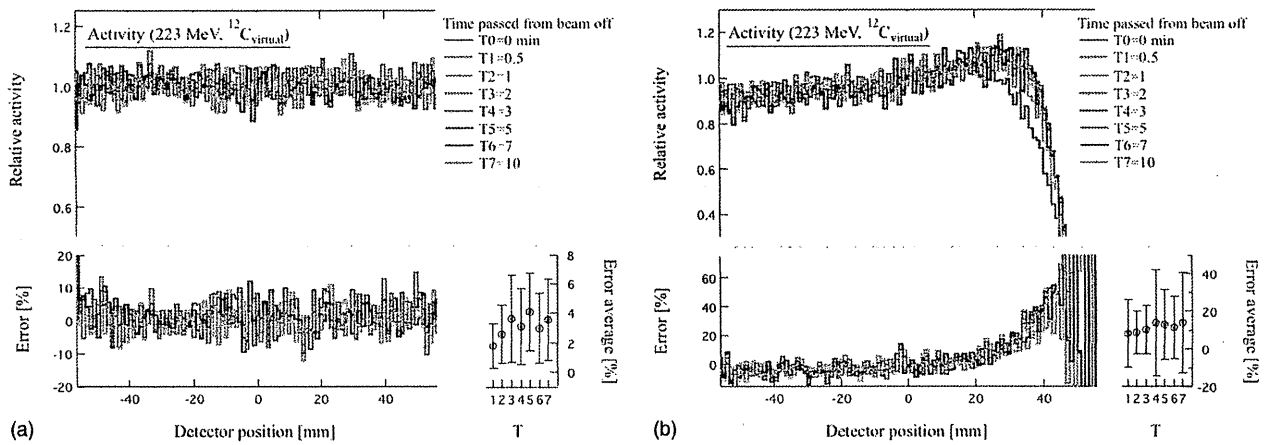
FIG. 4. Depth activity distributions of $^{12}C_{virtual}$ nuclei by starting time of measurement after 223 MeV proton beam irradiation to PE target are shown. (a) The area around entrance of PE target with incident proton beam and (b) the area around the proton beam range of 223 MeV. The lower right-hand graph showed the average error and deviation to data of T0 ($Ts = 0$).

As for the activity distribution around the beam range in Fig. 4(b), it can be observed that the range of the depth activity distribution at $Ts = 0$ is shallower than the other six distributions with Ts greater than 1 min. One neutron is generated by the reaction to generate a ^{11}C nucleus, and two neutrons are generated by the reaction to generate a ^{10}C nucleus in the target fragment reaction between ^{12}C nuclei and proton. The reaction to generate a ^{10}C nucleus needs more proton energy to generate a neutron than the reaction to generate a ^{11}C nucleus. Therefore, it can be considered that the range of depth activity distributions formed mainly from the information of ^{10}C nuclei was shallower than the distributions of the others. Moreover, it was observed that there was hardly a difference in depth activity distributions for Ts greater than 1 min. This may suggest that the quantitative proportion of generated ^{10}C nuclei to $^{12}C_{virtual}$ nuclei was small.

III.B.2. Half-lives of virtual positron emitter nuclei ($^{12}C_{virtual}$, $^{16}O_{virtual}$, and $^{40}Ca_{virtual}$)

It turned out that the simulation of activity distributions had to take the time dependence of the form of depth activity distributions into consideration given the result of Sec. III B 1 above. Therefore, the change of activity-intensity at each depth point with the passage of time was analyzed for the measured activity distributions for every target nucleus. The decay curves of measured activity data during the period of measurement (about 5 h) in a very small volume, which was set up around the depth point in the target, were obtained and the characteristics of the decay curves were identified. 10–16 points for analysis were set up and all targets and energies were analyzed in consideration of the form of the measured activity distribution. Figure 5 shows the result about $^{12}C_{virtual}$ nuclei by irradiation of 223 MeV proton beam.

The virtual positron emitter nuclei generated by proton irradiation were roughly divided into two elements by the length of the nucleus half-life for all the target nuclei in this study. The two kinds of nuclei whose half-lives are 20 min (^{11}C nucleus) and 20 s (^{10}C nucleus) are generated from ^{12}C nuclei as target nuclei, in the same way, 10–20 min (^{11}C and

^{13}N nuclei) and several minutes or under (^{15}O, ^{14}O, and ^{10}C nuclei) are done from ^{16}O nuclei and under 1 s (^{38}Ca and ^{39}Ca nuclei) and several minutes (^{38}K nuclei) are done from ^{40}Ca nuclei. Therefore, the decay curves of measured activity data in small volumes, which were set up for every depth point for analysis using Eq. (3) constructed with elements separated into two groups of half-lives, were approximated.

$$N_{act.}(z, t) = A_{T_{long}}(z) \cdot \left(\frac{1}{2}\right)^{\frac{t}{T_{long}(z)}}$$

$$+ A_{T_{short}}(z) \cdot \left(\frac{1}{2}\right)^{\frac{t}{T_{short}(z)}}. \tag{3}$$

Here, $N_{act.}$ represents measured activity data, t measurement time, T_{long} and T_{short} half-lives, and $A_{T_{long}}$ and $A_{T_{long}}$ total measured activity of each half-life. N_{act} is total measured activity at $t = 0$. Figure 5 shows the decay curves that were obtained from measured activity data of $^{12}C_{virtual}$ nuclei using 223 MeV proton beam and the fitting curves at 10
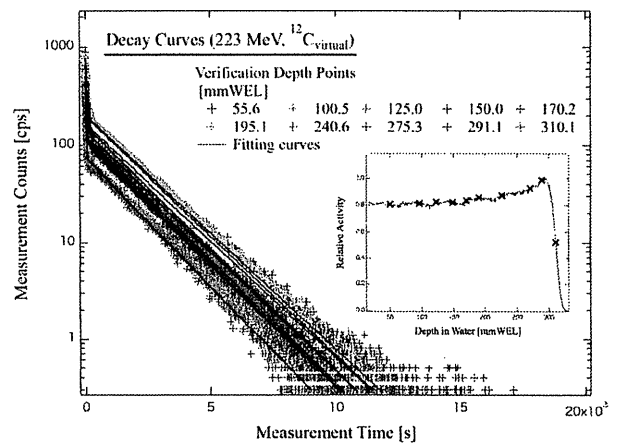

FIG. 5. The decay curves of measured activity data of $^{12}C_{virtual}$ nuclei during the measurement period (about 5 h) and the curves approximated using Eq. (3) in a very small volume at each depth point (223 MeV, PE target).

TABLE I. The results of approximation with two elements for each target and energy to the depth.

Target	Energy [MeV]	$R_{T_{long}}(\pm\Delta R_{T_{long}})$	$T_{long}(\pm\Delta T_{long})$ [s]	$\Delta R_{T_{long}}/R_{T_{long}}$ [%]	$\Delta T_{long}/T_{long}$ [%]
^{12}C	223	0.274 ($\pm$0.030)	1201 ($\pm$30)	10.8	2.5
	179	0.313 ($\pm$0.073)	1215 ($\pm$12)	23.4	1.0
	138	0.337 ($\pm$0.085)	1208 ($\pm$8)	25.2	0.7
^{16}O	223	0.029 ($\pm$0.011)	1354 ($\pm$339)	38.4	25.1
	179	0.030 ($\pm$0.007)	1257 ($\pm$74)	22.4	5.9
	138	0.036 ($\pm$0.011)	1078 ($\pm$69)	29.6	6.4
^{40}Ca	223	0.003 ($\pm$0.001)	582 ($\pm$84)	28.7	14.4
	179	0.002 ($\pm$0.000)	631 ($\pm$57)	24.7	9.1
	138	0.002 ($\pm$0.001)	576 ($\pm$36)	23.0	6.2

Target	Energy [MeV]	$R_{T_{short}}(\pm\Delta R_{T_{short}})$	$T_{short}(\pm\Delta T_{short})$ [s]	$\Delta R_{T_{short}}/R_{T_{short}}$ [%]	$\Delta T_{short}/T_{short}$ [%]
^{12}C	223	0.726 ($\pm$0.030)	20 ($\pm$3)	4.1	14.2
	179	0.687 ($\pm$0.073)	20 ($\pm$1)	10.7	3.5
	138	0.663 ($\pm$0.085)	19 ($\pm$1)	12.8	3.3
^{16}O	223	0.971 ($\pm$0.011)	139 ($\pm$6)	1.2	4.6
	179	0.970 ($\pm$0.007)	132 ($\pm$2)	0.7	1.5
	138	0.964 ($\pm$0.011)	126 ($\pm$2)	1.1	1.3
^{40}Ca	223	0.997 ($\pm$0.001)	1 ($\pm$0)	0.1	13.0
	179	0.998 ($\pm$0.000)	1 ($\pm$0)	0.0	7.0
	138	0.998 ($\pm$0.001)	1 ($\pm$0)	0.1	7.1

depth points. Fitting results of decay curves for each target and energy at the depth points were summarized in Table I.

The elements with short half-lives were approximated with higher accuracy than the elements with long half-lives in terms of both half-lives and ratios of these elements in the decay curves obtained from the measured activity data. Probably, the virtual positron emitter nuclei with short half-life had greater influence on the quantity of activity originating from virtual positron emitter nuclei, which might be detected immediately after proton irradiation (that is, $N_{act}.(z, t = 0)$), than the virtual positron emitter nuclei with a long half-life. Table I suggests that the activity distributions obtained immediately after proton irradiation were formed by the activity that originated from virtual positron emitter nuclei with short half-lives mainly for all targets and energies. About 30% of activity distributions of ^{12}C$_{virtual}$ nuclei were contributed to by the activity of virtual positron emitter nuclei with long half-lives, and the contributions to activity distributions of ^{16}O$_{virtual}$ nuclei and activity distributions of ^{40}Ca$_{virtual}$ nuclei were only a few percent.

The kinds of nuclei that contributed to measured activity data could be inferred from the approximated half-lives shown in Table I. T_{long} and T_{short} were about 20 min and 20 s for the approximate results of measured activity data of ^{12}C$_{virtual}$ nuclei, respectively, which suggested the existence of ^{11}C nuclei and

^{10}C nuclei. From T_{long} being around 20 min, the measured activity data of ^{16}O$_{virtual}$ nuclei might have mainly been contributed to by ^{11}C nuclei and various generated positron emitter nuclei such as ^{13}N nuclei (half-life: about 10 min). In addition, from T_{short} being around 130 s, it was estimated that many ^{15}O nuclei and a few other nuclei contributed to the measured activity data of ^{16}O$_{virtual}$ nuclei. As for the results of ^{40}Ca$_{virtual}$ nuclei, the existence of ^{38}K nuclei (half-life: about 8 min) was suggested from T_{long} being about 10 min and that of ^{38}Ca nuclei (half-life: 0.45 s) and ^{39}Ca nuclei (half-life: 0.86 s) from T_{short} being 1 s. The nuclei whose half-lives were under 1 s, such as ^{38}Ca nuclei and ^{39}Ca nuclei, were both approximated as one nuclei whose half-life was 1 s because the output of the measurement using BOLPs-RGp was every 1 s. In these circumstances, it is easy to distinguish the nuclei with short half-lives from the virtual positron emitter nuclei because half-lives of the generated positron emitter nuclei, which were classified as the virtual positron emitter nuclei with short half-lives, were especially short. It could be considered that the approximate accuracy of the elements with short half-lives was high for the reasons stated above.

Figure 6 shows plots of parameter, $A_{T_{long}}, A_{T_{short}}$, T_{long}, T_{short}, calculated using Eq. (3) for each target nucleus at 179 MeV proton beam. The activity ratios of ^{12}C$_{virtual}$, ^{16}O$_{virtual}$, and ^{40}Ca$_{virtual}$ nuclei were calculated using Eq. (4)

$$R_{T_{long}, T_{short}}(X_{virtual}; z) \equiv \frac{A_{T_{long}, T_{short}}(X_{virtual})}{N_{act}.(z, t = 0)} = \begin{cases} a(X_{virtual}) + \dfrac{b(X_{virtual})}{1 + \left(\dfrac{c(X_{virtual})}{z}\right)^{k(X_{virtual})}}, & (X_{virtual} = {}^{12}C_{virtual}) \\ a(X_{virtual}) + b(X_{virtual}) \cdot z^{k(X_{virtual})}, & (X_{virtual} = {}^{16}O_{virtual}) \\ a(X_{virtual}). & (X_{virtual} = {}^{40}Ca_{virtual}) \end{cases} \tag{4}$$
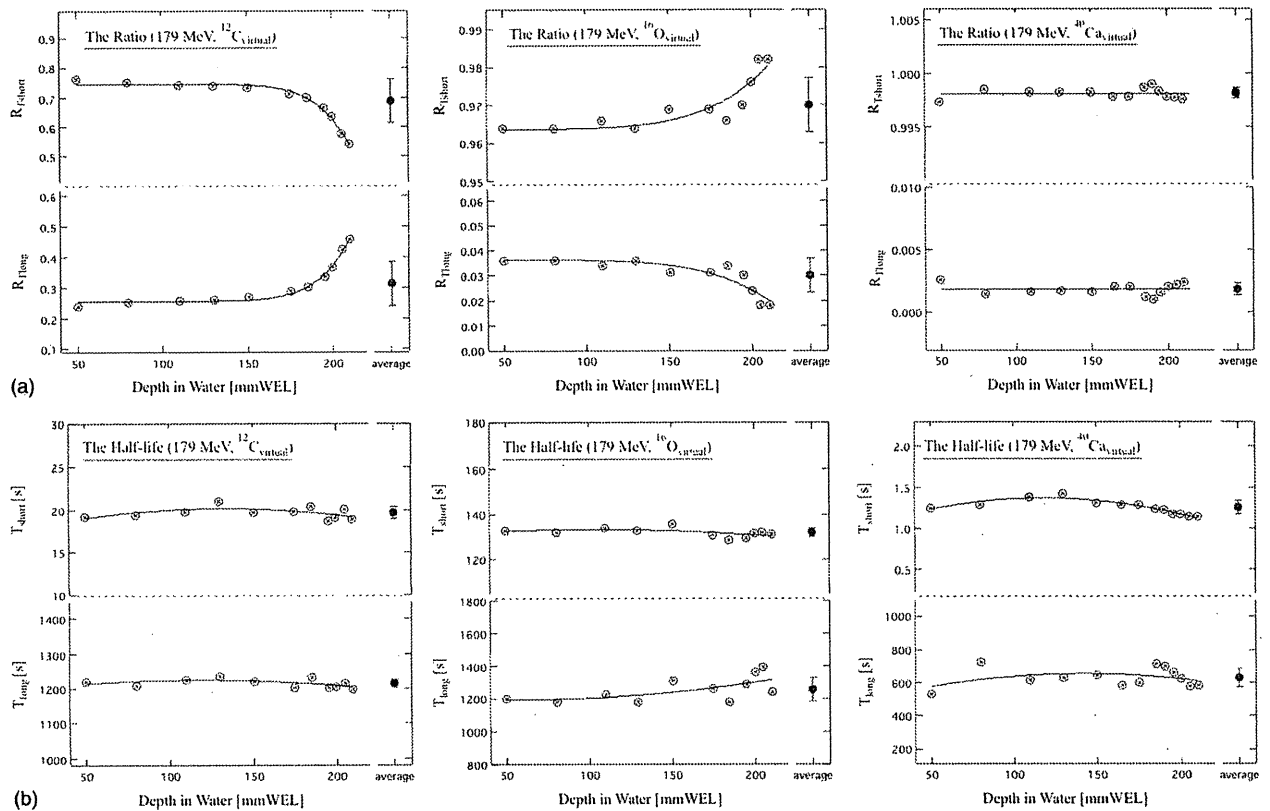
FIG. 6. The plotted points were the results that were the ratio of each half-life group of elements (a) and the hail-lives (b) approximated using Eq. (3) for each virtual positron emitter nuclei at 179 MeV. The curves approximated the results of approximation using Eqs. (4) and (5).

Here, $R_{T_{long},T_{short}}$ is the ratio of $X_{virtual}$ nucleus with each half-life element, and a, b, c, k are free parameters for fitting of data in each equation. The measured activity distributions of $^{40}Ca_{virtual}$ nuclei were mainly formed by the elements of short half-lives according to the result of ratio of ^{40}Ca nuclei half-life elements (see Table I). The half-lives both long and short were calculated using Eq. (5) for each virtual positron emitter nuclei.

$$T_{long,short}(X_{virtual}; z) = a(X_{virtual}) + b(X_{virtual}) \cdot z + c(X_{virtual}) \cdot z^2. \tag{5}$$

Here, $T_{long,short}$ is each half-life of $X_{virtual}$ nucleus. Table II shows the fitting results for each target and energy. The values that were obtained from measured activity data were widely distributed because the analysis volume was set up as small as possible to verify the depth dependence. This could explain why the points that were the results of that analysis are diffusely spread in Fig. 6. Therefore, the change of the form of depth activity distributions with the depth dependence was considered by using of the Eqs. (4) and (5) decided by the results of each target nucleus in this study.

Three nuclei, ^{12}C, ^{16}O, and ^{40}Ca, were proposed to be the main components related to the imaging of proton-irradiated volume in a patient body in this study. It was found that the elements with a short half-life for each target nucleus mainly affected the activity distributions of virtual positron emitter nuclei obtained by proton irradiation to all target nuclei. In

other words, it was suggested that the activity distributions obtained by proton irradiation of human body tissues, which were regarded as being mainly composed of ^{12}C nuclei, ^{16}O nuclei, and ^{40}Ca nuclei, were approximated by three half-life elements. It was reported that the activity distributions obtained by proton irradiation of human body tissues in clinical therapy could be approximated by three half-life elements, as found in our previous study.[2] It could be said that the results of this study to analyze three target nuclei (^{12}C, ^{16}O, and ^{40}Ca) have a strong relationship to the results of the previous study on clinical data.

III.C. Activity pencil beam kernel using measured depth activity distributions

Activity pencil beam kernel was constructed by the measured depth activity distribution data of virtual positron emitter nuclei and calculated lateral distributions of Gauss form considering the effect of multiple Coulomb scattering. The measured depth activity distribution data included the influence of time and depth dependence. Form of activity pencil beam kernel was decided by each energy of incident proton beam and each nucleus of ^{12}C, ^{16}O, and ^{40}Ca. And, the data were prepared for installing the simulation system of activity distributions. Figure 7 shows calculation results of the activity pencil beam kernel of $^{12}C_{virtual}$, $^{16}O_{virtual}$, and $^{40}Ca_{virtual}$ nuclei with mono-energetic proton beam of 179 MeV. There

TABLE II. The results of approximation using Eqs. (4) and (5) for each target and energy.

Target	Energy [MeV]	$R_{T_{long}}$			
		a	b	c	k
^{12}C	223	0.262	0.124	301.3	33.9
	179	0.255	2.757	258.0	12.2
	138	0.274	3.471	185.1	8.3
		a	b	k	
^{16}O	223	0.040	0.000	5.1	
	179	0.036	0.000	5.8	
	138	0.044	0.000	5.9	
		Constant Value			
^{40}Ca	223	0.003			
	179	0.002			
	138	0.002			

Target	Energy [MeV]	$R_{T_{short}}$			
		a	b	c	k
^{12}C	223	0.604	0.134	303.4	-31.3
	179	-0.888	1.633	244.8	-12.6
	138	-1.811	2.537	177.0	-8.4
		a	b	k	
^{16}O	223	0.960	0.000	5.1	
	179	0.964	0.000	5.8	
	138	0.956	0.000	5.9	
		Constant Value			
^{40}Ca	223	0.997			
	179	0.998			
	138	0.998			

Target	Energy [MeV]	T_{long}		
		a	b	c
^{12}C	223	1194.5	0.448	-0.002
	179	1192.7	0.531	-0.002
	138	1216.8	-0.308	0.002
^{16}O	223	1085.6	4.778	-0.014
	179	1210.5	-0.588	0.005
	138	1113.1	-2.343	0.019
^{40}Ca	223	813.3	-2.870	0.007
	179	471.1	2.593	-0.009
	138	578.5	0.402	-0.004

Target	Energy [MeV]	T_{short}		
		a	b	c
^{12}C	223	16.4	0.081	0.000
	179	17.2	0.045	0.000
	138	17.7	0.031	0.000
^{16}O	223	139.6	0.078	0.000
	179	130.5	0.052	0.000
	138	129.1	-0.114	0.001
^{40}Ca	223	1.4	0.001	0.000
	179	1.0	0.007	0.000
	138	1.1	0.000	0.000

are four graphs of depth activity distributions, coefficient of multiple Coulomb scattering to depth (1σ), two-dimensional activity pencil beam kernel, and depth activity distributions toward the distance from the central proton beam axis shown in Fig. 7.

The pencil beam algorithm takes into consideration the way in which the center of the proton beam passes through inhomogeneous material in calculation of proton dose distribution. However, lateral Gaussian distribution only represents the scatter in water with no density gap. The accuracy of calculation deteriorates at the point with a large density gap in the inhomogeneous area composed of matter with various densities, such as bone and air. The same phenomenon occurs in the APB algorithm. On the other hand, research to improve the accuracy of the pencil beam algorithm has been carried out worldwide. Calculation using the pencil beam algorithm is being developed to a higher level of accuracy. For instance, research is being carried out on the development of the calculation algorithm with high accuracy on the border of inhomogeneous matter by regarding a scattered beam after passing fine degrader and bolus as a thin beam.[27] The calculation accuracy of activity distributions using the APB algorithm is the same as the calculation accuracy of dose distributions in clinical proton therapy. Therefore, it is evaluated that the calculation accuracy using the APB algorithm satisfies the accuracy required in clinical use. With progress in the research and development on improving the accuracy of dose calculation, mainly using the pencil beam algorithm, it is certain that the accuracy of activity distribution calculation using the APB algorithm will also be improved. In these circumstances and given these future possibilities, it will be very valuable for calculation of activity distributions to utilize the pencil beam algorithm.

III.D. Sorting CT image of patients into composite nuclear image in a human body for simulation of activity distributions

In proton dose calculation, the physical process of a proton beam passing into a human body is based on electromagnetic interaction, which is mainly proportional to the ionization potential of matter depended on the atomic number Z. In addition, the CT value of a CT image taken for the physical reactions of Photoelectric effect and Compton scattering between a human body and x-ray of about 100 kV depends on the electron density of matter depended on Z. Using these relationships with Z, proton dose distributions are calculated using CT image of patient for treatment planning in clinical proton therapy. On the other hand, target nuclear fragment reactions, which are nuclear reactions between atomic nuclei that constitute a human body and proton in proton therapy, are related to the atomic number Z and the mass number A, as an nucleus is identified by these factors of Z and A. Therefore, sorting the CT image of patients into nuclei is essential to simulate imaging of the planned irradiation volume, although it is suggested that calculation with high speed and high accuracy using APB algorithm can be used in a clinical routine. The best approach is
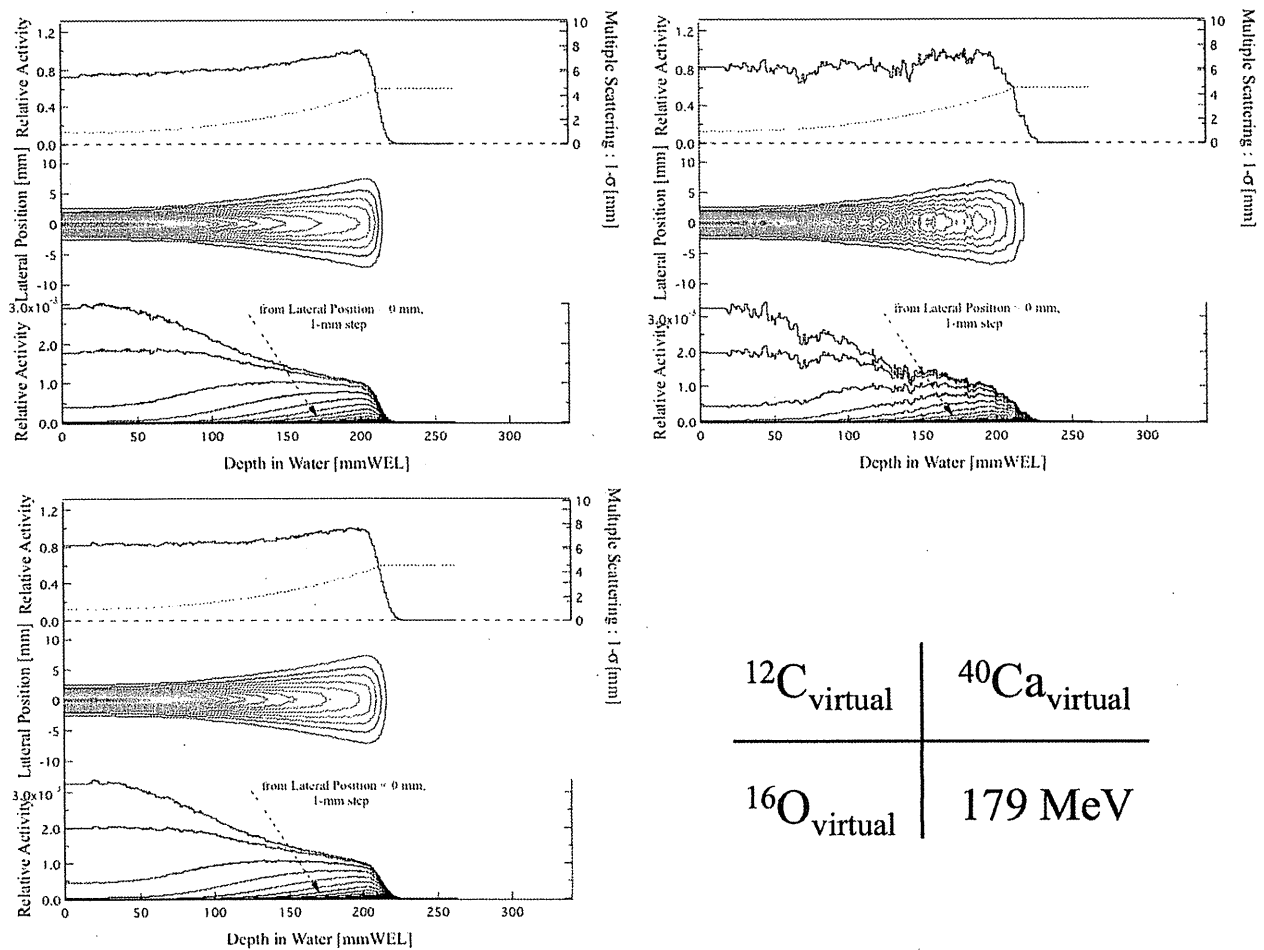
FIG. 7. The results of calculated activity pencil beam kernel of $^{12}C_{virtual}$, $^{16}O_{virtual}$, and $^{40}Ca_{virtual}$ nuclei with mono-energetic proton beam of 179 MeV. There are four graphs, the upper: depth activity distributions and coefficient of multiple Coulomb scattering to depth (1σ), the middle: two-dimensional activity pencil beam kernel, the lower: depth activity distributions toward the distance from the central proton beam axis. .

that sorting of CT images into nuclei is done on an individual patient because the composition of human body tissue differs among individuals. However, such a technique has not been established yet. The accuracy of identifying human body tissue from CT values affects the accuracy of dose calculation in proton therapy.[28,29] Research on the relationship between CT value and human body tissue to improve the accuracy of dose and activity calculations in proton therapy has been continuously done.[15,16,29–33] The accuracy of identifying nuclei in the human body from CT images has a strong relationship to the accuracy of the whole simulation of imaging of the planned irradiation volume. Therefore, which technique of identification is to be chosen is an issue to be resolved.

IV. CONCLUSIONS

The APB algorithm that has both the accuracy and the calculation time required for clinical use was developed as a new calculation algorithm for the simulation of activity distributions. It was expected that a simulation system with the APB algorithm for making activity distributions of irradiated

volume in patient body using activity pencil beam kernel could be put into clinical use.

It was found that three target nuclei, ^{12}C, ^{16}O, and ^{40}Ca, were important and appropriate for calculation of activity distributions by verification and analysis of clinical data in this study. In terms of the information of target nuclear fragment reactions between proton and nuclei in a human body required for calculation of activity distributions, the information of reactions was enriched with the measured data of the generated virtual positron emitter nuclei to improve the accuracy of simulation of activity distributions. Acquisition of the data of target nuclear fragment reactions between ^{40}Ca nuclei and proton within the range of energy used for proton therapy in this study was very useful because such data are limited at present. Moreover, high accurate proton therapy can be provided by the development of a new calculation algorithm considering the time and depth dependence of the forms of activity distributions.

We have been constructed a simulation system of imaging of proton-irradiated volume equipped the APB algorithm now. Then, it will be possible to verify the changes of the irradiated volume and the influence of washout effect on

images of activity distributions by comparing the results of calculation with measurement using BOLPs-RGp. It is thought that there are many seeds (e.g., *in vivo* dosimetry) of research based on measurement and calculation of activity in irradiated volume. The accuracy of activity distribution calculation using APB algorithm is future problem. Therefore, it will be important for verification of measured activity distribution using BOLPs-RGp and calculated activity distribution using APB algorithm in clinical cases. It is expected that the APB algorithm can be utilized for proton therapy with imaging of irradiated volume. We will be able to provide high quality proton therapy for patients.

ACKNOWLEDGMENTS

a)Electronic mail: miyatake.keenmps@gmail.com

[1]T. Nishio, A. Miyatake, T. Ogino, K. Nakagawa, N. Saijo, and H. Esumi, "The development and clinical use of a beam ON-LINE PET system mounted on a rotating gantry port in proton therapy," Int. J. Radiat. Oncol., Biol., Phys. **76**, 277–286 (2010).

[2]A. Miyatake, T. Nishio, T. Ogino, N. Saijo, H. Esumi, and M. Uesaka, "Measurement and verification of positron emitter nuclei generated at each treatment site by target nuclear fragment reactions in proton therapy," Med. Phys. **37**, 4445–4455 (2010).

[3]G. W. Bennett, A. C. Goldberg, G. S. Levine, J. Guthy, and J. Balsamo, "Beam localization via 15O activation in proton-radiation therapy," Nucl. Instrum. Methods **125**, 333–338 (1975).

[4]U. Oelfke, G. Lam, and M. Atkins, "Proton dose monitoring with PET: Quantitative studies in Lucite," Phys. Med. Biol. **41**, 177–196 (1996).

[5]D. W. Litzenberg, D. A. Roberts, M. Y. Lee, K. Pham, A. M. Vander Molen, R. Ronningen, and F. D. Becchetti, "On-line monitoring of radiotherapy beams: Experimental results with proton beams," Med. Phys. **26**(6), 992–1006 (1999).

[6]T. Nishio, T. Ogino, M. Shimbo, S. Katsuta, S. Kawasaki, T. Murakami, T. Sato, Y. Kojima, K. Murakami, and H. Ikeda, "Distributions of β^+ decayed nucleus produced from the target fragment reaction in $(CH_2)n$ and patient liver targets by using a proton beam for therapy," *Abstracts of the XXXIV PTCOG MEETING in Boston*, p. 15–16 (2001).

[7]Y. Hishikawa, K. Kagawa, M. Murakami, H. Sasaki, T. Akagi, and M. Abe, "Usefulness of positron-emission tomographic images after proton therapy," Int. J. Radiat. Oncol., Biol., Phys. **53**, 1388–1391 (2002).

[8]W. Enghardt, P. Crespo, F. Fiedler, R. Hinz, K. Parodi, J. Pawelke, and F. Ponisch, "Dose quantification from in-beam positron emission tomography," Radiother. Oncol. **73**, Suppl. 2. S96–98 (2004).

[9]T. Nishio, T. Sato, H. Kitamura, K. Murakami, and T. Ogino, "Distributions of β^+ decayed nuclei generated in the CH_2 and H_2O targets by the target nuclear fragment reaction using therapeutic MONO and SOBP proton beam," Med. Phys. **32**(4), 1070–1082 (2005).

[10]T. Nishio, T. Ogino, K. Nomura, and H. Uchida, "Dose-volume delivery guided proton therapy using beam ON-LINE PET system," Med. Phys. **33**(11), 4190–4197 (2006).

[11]T. Nishio, A. Miyatake, K. Inoue, S. Katsuta, T. Gomi-Miyagishi, R. Kohno, S. Kameoka, K. Nakagawa, and T. Ogino, "Experimental verification of proton beam monitoring in a human body by use of activity image of positron-emitting nuclei generated by nuclear fragmentation reaction," Radiol. Phys. Technol. **1**(1), 44–54 (2008).

[12]K. Parodi and W. Enghardt, "Potential application of PET in quality assurance of proton therapy," Phys. Med. Biol. **45**, N151–N156 (2000).

[13]K. Parodi, W. Enghardt, and T. Haberer, "In-beam PET measurements of β^+ radioactivity induced by proton beams," Phys. Med. Biol. **47**, 21–36 (2002).

[14]K. Parodi, F. Ponisch, and W. Enghardt, "Experimental study on the feasibility of in-beam PET for accurate monitoring of proton therapy," IEEE Trans. Nucl. Sci. **52**, 778–786 (2005).

[15]K. Parodi, H. Paganetti, H. A. Shih, S. Michaud, J. S. Loeffler, T. F. Delaney, N. J. Liebsch, J. E. Munzenrider, A. J. Fischman, A. Knopf, and T. Bortfeld, "Patient study of in vivo verification of beam delivery and range, using positron emission tomography and computed tomography imaging after proton therapy," Int. J. Radiat. Oncol., Biol., Phys. **68**(3), 920–934 (2007).

[16]K. Parodi, H. Paganetti, E. Cascio, J. B. Flanz, A. A. Bonab, N. M. Alpert, K. Lohmann, and T. Bortfeld, "PET/CT imaging for treatment verification after proton therapy: A study with plastic phantoms and metallic implants," Med. Phys. **34**(2), 419–435 (2007).

[17]K. Parodi, A. Ferrari, F. Sommerer, and H. Paganetti, "Clinical CT-based calculations of dose and positron emitter distributions in proton therapy using the FLUKA Monte Carlo code," Phys. Med. Biol. **52**, 3369–3387 (2007).

[18]S. Agostinelli *et al.*, "(GEANT4 Collaboration) 2003 GEANT4: a simulation toolkit," Nucl. Instrum. Methods Phys. Res. A **506**, 250–303 (2003).

[19]J. Allison *et al.*, "(GEANT4 Collaboration) 2006 GEANT4 developments and applications," IEEE Trans. Nucl. Sci. **53**, 270–278 (2006).

[20]A. Fassò, A. Ferrari, J. Ranft, and P. Sala, FLUKA-98 (http://www.oecd-nea.org/science/iend.hide/iend_20.pdf) (1998).

[21]F. Ponisch, K. Parodi, B. G. Hasch, and W. Enghardt, "The modelling of positron emitter production and PET imaging during carbon ion therapy," Phys. Med. Biol. **49**, 5217–5232 (2004).

[22]NNDC : http://www.nndc.bnl.gov./

[23]G. Moliere, "Theorie der Streuung schneller geladener Teilchen II," Nucl. Instrum. Methods Phys. Res. B **74**, 467–490 (1948).

[24]L. V. Highland, "Some practical remarks on multiple scattering," Nucl. Instr. Methods **129**, 467–499 (1975).

[25]R. G. Lynch and I. O. Dahl, "Approximations to multiple Coulomb scattering," Nucl. Instrum. Methods Phys. Res. B **58**, 6–10 (1991).

[26]M. Hollmark *et al.*, "Influence of multiple scattering and energy loss straggling on the absorbed dose distributions of therapeutic light ion beams: I. Analytical pencil beam model," Phys. Med. Biol. **49**, 3247–3265 (2004).

[27]N. Kanematsu, "Semi-empirical formulation of multiple scattering for the Gaussian beam model of heavy charged particles stopping in tissue-like matter," Phys. Med. Biol. **54**, N67–N73 (2009).

[28]B. Schaffner and E. Pedroni, "The precision of proton range calculations in proton radiotherapy treatment planning: experimental verification of the relation between CT-HU and proton stopping power," Phys. Med. Biol. **43**, 1579–1592 (1998).

[29]H. Jiang, J. Seco, and H. Paganetti, "Effects of Hounsfield number conversions on patient CT based Monte Carlo proton dose calculation," Med. Phys. **34**, 1439–1449 (2007).

[30]H. Jiang and H. Paganetti, "Adaptation of GEANT4 to Monte Carlo dose calculations based on CT data," Med. Phys. **31**, 2811–2818 (2004).

[31]H. Paganetti, H. Jiang, K. Parodi, R. Slopsema, and M Engelsman, "Clinical implementation of full Monte Carlo dose calculation in proton beam therapy," Phys. Med. Biol. **53**, 4825–4853 (2008).

[32]H. Paganetti, "Dose to water versus dose to medium in proton beam therapy," Phys. Med. Biol. **54**, 4399–4421 (2009).

[33]S. Espana and H. Paganetti, "The impact of uncertainties in the CT conversion algorithm when predicting proton beam ranges in patients from dose and PET-activity distributions," Phys. Med. Biol. **55**, 7557–7571 (2010).

doi:10.1016/j.ijrobp.2010.08.009

CLINICAL INVESTIGATION

PROTON BEAM THERAPY FOR UNRESECTABLE MALIGNANCIES OF THE NASAL CAVITY AND PARANASAL SINUSES

SADAMOTO ZENDA, M.D.,* RYOSUKE KOHNO, PH.D.,* MITSUHIKO KAWASHIMA, M.D.,*
SATOKO ARAHIRA, M.D.,* TEIJI NISHIO, PH.D.,* MAKOTO TAHARA, M.D., PHD.,[†] RYUICHI HAYASHI, M.D.,[‡]
SEIJI KISHIMOTO, M.D., PH.D.,[§] AND TAKASHI OGINO, M.D.*

Division of *Radiation Oncology, [†]Gastrointestinal Oncology and Endoscopy, and [‡]Head and Neck Surgery, National Cancer Center Hospital East, Chiba, Japan; and [§]Department of Head and Neck Surgery, Tokyo Medical and Dental University, Tokyo, Japan

Purpose: The cure rate for unresectable malignancies of the nasal cavity and paranasal sinuses is low. Because irradiation with proton beams, which are characterized by their rapid fall-off at the distal end of the Bragg peak and sharp lateral penumbra, depending on energy, depth, and delivery, provide better dose distribution than X-ray irradiation, proton beam therapy (PBT) might improve treatment outcomes for conditions located in proximity to risk organs. We retrospectively analyzed the clinical profile of PBT for unresectable malignancies of the nasal cavity and paranasal sinuses.
Methods and Materials: We reviewed 39 patients in our database fulfilling the following criteria: unresectable malignant tumors of the nasal cavity, paranasal sinuses or skull base; N0M0 disease; and treatment with PBT (>60 GyE) from January 1999 to December 2006.
Results: Median patient age was 57 years (range, 22–84 years); 22 of the patients were men and 17 were women. The most frequent primary site was the nasal cavity (n = 26, 67%). The local control rates at 6 months and 1 year were 84.6% and 77.0%, respectively. With a median active follow-up of 45.4 months, 3-year progression-free and overall survival were 49.1% and 59.3%, respectively. The most common acute toxicities were mild dermatitis (Grade 2, 33.3%), but no severe toxicity was observed (Grade 3 or greater, 0%). Five patients (12.8%) experienced Grade 3 to 5 late toxicities, and one treatment-related death was reported, caused by cerebrospinal fluid leakage Grade 5 (2.6%).
Conclusion: These findings suggest that the clinical profile of PBT for unresectable malignancies of the nasal cavity and paranasal sinuses make it is a promising treatment option. © 2010 Elsevier Inc.

Proton beam therapy, nasal cavity, paranasal sinus, radiotherapy, craniofacial surgery, organ preservation.

INTRODUCTION

Malignant tumors that arise in the nasal or paranasal sinuses and that otherwise involve the base of the skull usually present a difficult clinical problem. Most cases are curatively treated by craniofacial surgery and postoperative radiotherapy, either alone or in combination (1–5). However, several problems with this strategy remain. In cases in which the disease has spread deeply to the intracranial region, surgical approaches are often complicated by serious functional deformity, and satisfactory surgical clearance is often markedly difficult to obtain (6 ,7). For theses cases, definitive radiotherapy is often performed as an alternative treatment, but aggressive irradiation of the intracranial region increases the risk of severe late toxicity (8–10).

Proton beams are characterized by their rapid fall-off at the distal end of the Bragg peak and sharp lateral penumbra,

depending on energy, depth, and delivery (11). These physical characteristics give proton beam therapy (PBT) better dose distribution than X-ray irradiation, and PBT is now deemed a feasible and effective treatment modality that provides curative high-dose irradiation to the tumor volume without increasing normal tissue toxicity. However, few papers have described the use of PBT in unresectable malignancies of the nasal cavity and paranasal sinuses.

Here, we conducted a retrospective analysis to clarify the clinical profile of PBT for unresectable malignancies of the nasal cavity and paranasal sinuses.

METHODS AND MATERIALS

Patients

A total of 39 patients in our database fulfilling the following criteria were reviewed: unresectable malignant tumors of the nasal

cavity, paranasal sinuses, or skull base; no lymph node metastases or distant metastases; and treatment with definitive PBT (>60 GyE) from January 1999 to December 2006. Unresectable disease was defined as the inability of a surgeon to perform complete resection because of functional or technical limitations. Patients recruited for other clinical trials were excluded from this analysis.

Pretreatment evaluation

Pretreatment clinical evaluation was performed using magnetic resonance imaging (MRI), cervical, chest, and abdominal computed tomography (CT), or positron emission tomography (PET)–CT. Tumor staging in the present study was based on the sections on the nasal cavity and paranasal sinuses in the TNM classification of the International Union Against Cancer (UICC 6th), regardless of histology type. Radiological evaluations for staging were jointly reviewed by radiologists, head-and-neck surgeons, and medical oncologists at our institution.

Efficacy and toxicity evaluation

Overall survival was calculated from the start of treatment to the date of death or last confirmed date of survival. Progression-free survival (PFS) was defined as from the day of initiation of treatment to the first day of confirmation of progressive disease or death by any cause. Local control was defined as the lack of progressive disease at the primary site.

The pattern of treatment failure was defined as the first site of failure, with local failure indicating recurrence or persistent disease after PBT at the primary site, regional failure indicating neck lymph node metastases after PBT, and distant failure indicating recurrence at any site beyond the primary site and neck lymph nodes.

Acute and late toxicities were graded according to the Common Terminology Criteria for Adverse Events v3.0 (CTCAE v3.0). Time to onset of toxicity Grade 2 or greater was defined as from the day of initiation of treatment to the first day of confirmation of late toxicity of Grade 2 or greater.

Proton beam therapy

Treatment planning was performed on a three-dimensional CT planning system. In this system, the proton beam was generated with a Cyclotron C235 with an energy of 235 MeV at the exit. Relative biologic effectiveness was defined as 1.1, based on our preclinical experiments (12). Proton beam therapy at our institution is conducted using passive irradiation with dual-ring double-scatter methods. Dose distribution is optimized using the spread-out Bragg peak method and obtained using a broad-beam algorithm.

Gross tumor volume (GTV) was determined by pretreatment with CT, MRI, and PET-CT, either alone or in combination. Clinical target volume (CTV) was defined as the GTV plus a 5-mm margin and the sinuses adjacent to the GTV. In cases with brain invasion, the area of T2 prolongation on MRI was also included in the CTV. Planning target volume (PTV) was basically defined as the CTV plus a 3-mm margin but could be finely adjusted where necessary in consideration of organs at risk. Beam energy and spread-out Bragg peak were fine-tuned such that the PTV was at least covered in a 90% isodose volume of the prescribed dosage. The irradiated dose was minimized by delivery of the proton beam with two or three beam arrangements (Fig. 1). The biologically equivalent dose (BED) using a linear-quadratic model was defined as follows: BED $= nd\,(1+ d/\,1/(\alpha/\beta))$, where n is the fractionation number, d is the daily dose, and α/β ratio was 3.0 Gy for normal tissue (12).

Dose constraints for organs at risk at 2.5 GyE per fraction were as follows: (1) surface of brainstem, 51 GyE; (2) center of brainstem,
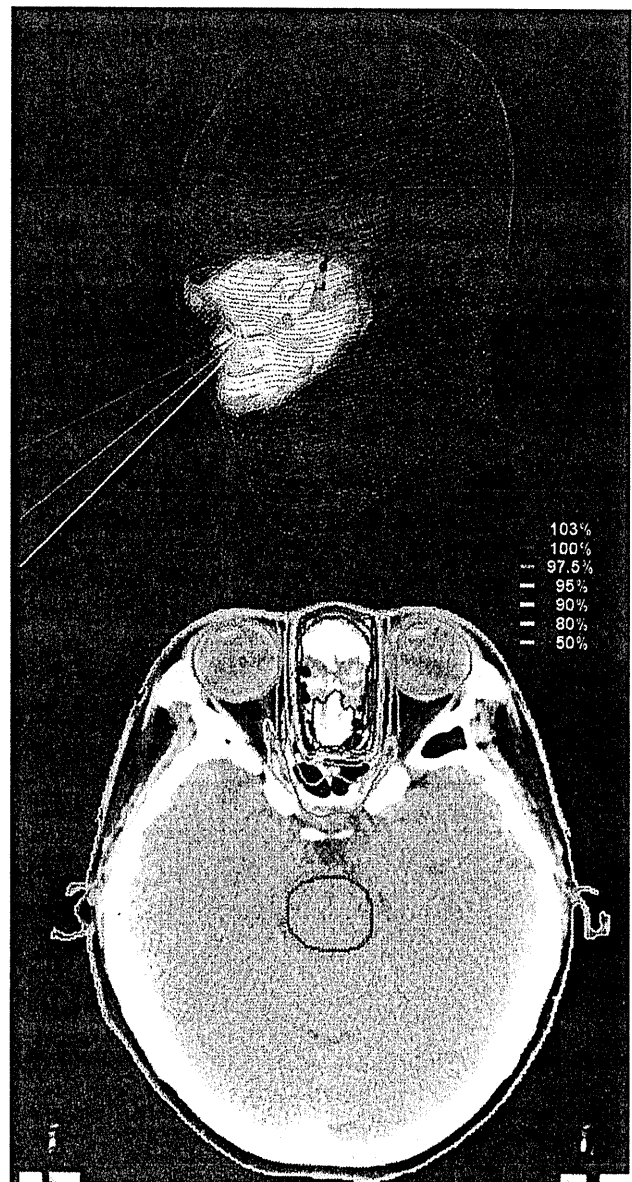

Fig. 1. Beam arrangement. Irradiation dose and volume for organs at risk was usually minimized using a noncoplanar three-field technique. In this case, curative high-dose irradiation to the tumor volume was provided, whereas overdose irradiation to the optic nerve was avoided.

46 GyE; (3) optic nerves of the healthy side/chiasm, 46 GyE; and (4) optic lens, 9 GyE.

Statistical analysis

Overall and progression-free survival time were estimated by the Kaplan–Meier product–limits method using commercially available statistical software (StatView version 5.0, SAS Institute, Cary, NC).

Univariate analysis was conducted using the log-rank test and multivariate analysis using the Cox proportional hazard model.

RESULTS

Patient characteristics

All patients had T4 disease and an Eastern Cooperative Oncology Group performance status of 0 or 1. Median age

was 57 years (range, 22–84 years). The major primary site was the nasal cavity (*n* = 26, 67%). One patient with squamous cell carcinoma from the ductus nasolacrimalis was included.

Regarding treatment, 10 patients received induction chemotherapy before PBT, whereas 29 patients had no prior treatment. One patient received PBT concurrent with cisplatin, whereas the remaining patients received PBT alone. The most common treatment was PBT alone at 65 GyE in 26 fractions. Patient characteristics are listed in Table 1.

Efficacy and failure pattern

With a median follow-up period of 45.4 months (range, 1.3–90.9 months), median survival time was not reached. The 3-year and 5-year overall survival rates were 59.3% and 55.0%, whereas the 3-year progress-free survival rate was 49.1% (Fig. 2).

Local control rates at 6 months and 1 year were 84.6% and 77.0%, respectively.

A total of 23 patients were confirmed to have tumor progression, consisting of 9 (23.0%), 5 (12.8%), and 9 (23.0%) patients with local, regional, and distant failure, respectively.
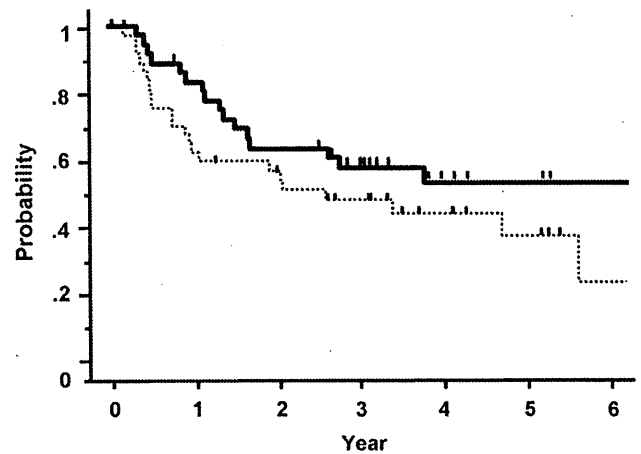

Fig. 2. Overall and progression-free survival. Solid line indicates overall survival curve; broken line indicates progression-free survival curve. With a median follow-up period of 45.4 months, 3-year overall survival and progression-free survival rates were 59.3% and 49.1%, respectively.

Time to the onset of local, regional and distant metastases was 9.4, 12.1, and 11.3 months, respectively. Nine of these patients (39.1%) received second-line treatment. Salvage surgery was performed for 1 patient with local failure and 3 patients with regional failure.

Prognostic factors

In univariate analysis, age, sex, tumor type (squamous cell carcinoma vs. others), primary site (nasal cavity vs. others), history of induction chemotherapy and RT dose were investigated (Table 2). Tumor type (squamous cell carcinoma) had

Table 1. Patient characteristics and treatment (*N* = 39)

Characteristic	*N*
Age, y (range)	57 (22–84)
Sex, male/female	22/17
Performance status	
0	25
1	14
2	0
Primary site	
Maxillary sinus	4
Sinonasal	4
Sphenoid sinus	4
Nasal cavity	26
Ductus nasolacrimalis	1
Tumor type	
SCC	11
ACC	5
ONB	9
Melanoma	6
Undifferentiated	3
Others	5
Treatment	
Induction chemotherapy	
Yes	10
No	29
Concurrent chemotherapy	
Yes (CDDP)	1
No	38
PBT dose schedule	
70 GyE/28 fr	3
70 GyE/35 fr	2
66 GyE/33 fr	1
65 GyE/26 fr	27
60 GyE/15 fr	6

Abbreviations: ACC = adenoid cystic carcinoma; CDDP = cisplatin; ONB = olfactory neuroblastoma; PBT = proton beam therapy; SCC = squamous cell carcinoma; Undif = undifferentiated carcinoma.

Table 2. Results of univariate analysis (*N* = 39)

Covariate	3-Year OS and PFS rates	Hazard ratio (95% CI)
Age		
OS		1.01 (0.99–1.04)
PFS		1.01 (0.98–1.04)
Sex (female vs. male)		
OS	62.5% vs. 56.9%	0.87 (0.34–2.21)
PFS	48.6% vs. 49.6%	1.17 (0.51–2.65)
Tumor type (SCC vs. other)		
OS	48.0% vs. 63.7%	2.17 (0.81–8.55)
PFS	40.0% vs. 52.1%	1.12 (0.45–2.85)
Primary site (nasal cavity vs. other)		
OS	69.2% vs. 37.0%	0.37 (0.15–0.95)
PFS	60.6% vs. 25.0%	0.55 (0.23–1.30)
Induction chemotherapy (yes vs. no)		
OS	70.0% vs. 56.7%	0.67 (0.22–2.05)
PFS	66.7% vs. 38.5%	0.50 (0.17–1.50)
Radiation dose		
OS		1.04 (0.88–1.22)
PFS		0.94 (0.81–1.08)

Abbreviations: BED = biologically equivalent dose; CI = confidence interval; OS = overall survival; PFS = progression-free survival; SCC = squamous cell carcinoma.

Table 3. Toxicity in study patients ($N = 39$)

	Grade (CTCAE v.3.0)					
	1	2	3	4	5	% 3–5
Dermatitis	17	13	0	0	0	0
Conjunctivitis	1	1	0	0	0	0
Mucositis	4	4	0	0	0	0
Hearing loss	0	1	0	0	0	0
Cataract	0	0	1	0	0	2.6
CSF leakage	0	0	0	0	1	2.6
Neuropathy						
CN-II	0	1	0	1	0	2.6
CN-VI	0	0	1	0	0	2.6
Brain necrosis	2	1	0	0	0	0
Soft tissue necrosis	0	0	0	0	0	0
Bone necrosis	0	2	1	0	0	2.6
Treatment-related death: 2.6%						

Abbreviations: CN = central nerve; CSF = cerebrospinal fluid; CTCAE v3.0 = common terminology criteria for adverse events v3.0.

a slight tendency to worsen overall survival, albeit without statistical significance ($p = 0.10$). The primary site (nasal cavity) had a significant influence on overall survival ($p = 0.04$). These two factors were subject to multivariate analysis, but no independent prognostic factors were identified.

Toxicity

Toxicity profile is summarized in Table 3. No severe acute toxicities were seen. The most common acute toxicities were dermatitis, with Grade 2 and 3 dermatitis occurring in 13 (33.3%) and 0 (0%) patients, respectively.

With regard to late toxicity, median time to onset of Grade 2 or greater late toxicity was 35.1 months (range, 4.1–61.2 months). Osteonecrosis caused by exodontia after PBT was observed in 2 patients. Occurrence of late toxicity was not significantly associated with age, gender, primary site, BED, or history of induction chemotherapy.

Grade 3 to 5 late toxicities occurred in 5 patients (12.8%), namely cerebrospinal fluid (CSF) leakage, cataract, decrease in visual acuity, central nerve–VI disorder, and bone necrosis in 1 patient each. One treatment-related death was recorded, caused by CSF leakage Grade 5 (2.6%). At the time of writing, 3 of the 5 patients with severe late toxicity remain alive. Severe toxicity after PBT is detailed in Table 4.

DISCUSSION

The present study suggests that the safety and efficacy profiles of PBT are sufficient for use in the treatment of unresectable malignancies of the nasal cavity and paranasal sinuses.

One strategy with curative intent is craniofacial surgery followed by radiotherapy. Complete surgical resection followed by postoperative radiotherapy has been shown to provide the best local control and overall survival in patients with nasal or paranasal sinuses carcinoma (2–5). In cases in which the status of the surgical margin is positive, however, the risk of recurrence is significantly high (6). These cases are often treated with radiotherapy as an alternative, but outcomes have remained poor (4, 10); in their series, for example, Hoppe *et al.* (10) reported a 5-year survival rate of definitive (chemo) radiotherapy for unresectable carcinoma of the paranasal sinuses of only 15%. Considerable improvement in treatment strategies for these conditions has therefore been sought.

In the present study, 3-year PFS and overall survival rates in patients treated with definitive PBT were 49.1% and 59.3%, respectively. Only 23.0% of all disease progression was local recurrence or persistence. These results are substantially better than those reported previously for radiotherapy and suggest that definitive PBT may be a promising treatment option for patients who are not candidates for surgery.

Response rate could not be shown in the present study. We consider that response evaluation for the primary site using the Response Evaluation Criteria in Solid Tumor (RECIST) criteria, complete response or partial response (CR/PR), is not useful with regard to nasal cavity and paranasal tumors because patients with long survival often show the persistence of the tumor form on CT or MRI after PBT (Fig. 3). On the other hand, local failure means disease progression at the primary site in CT or MRI after PBT, and local failure can be determined at any time if evidence of disease progression is seen.

On this basis, the present study shows the rate of local control and failure in place of response rate. A method that optimizes response evaluation for malignancy of the nasal cavity and paranasal sinuses is required.

In the present study, no factors associated with treatment outcome were detected. Although T stage and performance status are important factors influencing the treatment outcome of malignancies in various fields, all patients in our

Table 4. Late toxicity in study: Grade 3–4 (severe toxicity)

Case no.	Age (y)	Sex	Treatment	Tumor site	Toxicity	Time to onset	Recurrence	Status
11	58	Male	IC→PBT (70 GyE/28 fr)	Sphenoid sinus	Brain necrosis Grade 2 CN-VI disorder Grade 3	35.2 mo	None	Alive 65.6 mo
12	61	Female	IC→PBT (65 GyE/26 fr)	Nasal cavity	CSF leakage Grade 5	13.6 mo	None	Treatment-related death
25	63	Male	IC→PBT (65 GyE/26 fr)	Nasal cavity	Bone necrosis Grade 3	38.7 mo	None	Alive 45.4 mo
27	79	Male	PBT (60 GyE/15 fr)	Nasal cavity	Visual Loss Grade 4	16.6 mo	None	Alive 38.1 mo
30	73	Female	PBT (65 GyE/26 fr)	Nasal cavity	Cataract Grade 3	4.0 mo	Distant	Died 23.8 mo

Abbreviations: CSF = cerebrospinal fluid; CN = central nerve; fr = fractions; IC = induction chemotherapy; PBT = proton beam therapy.
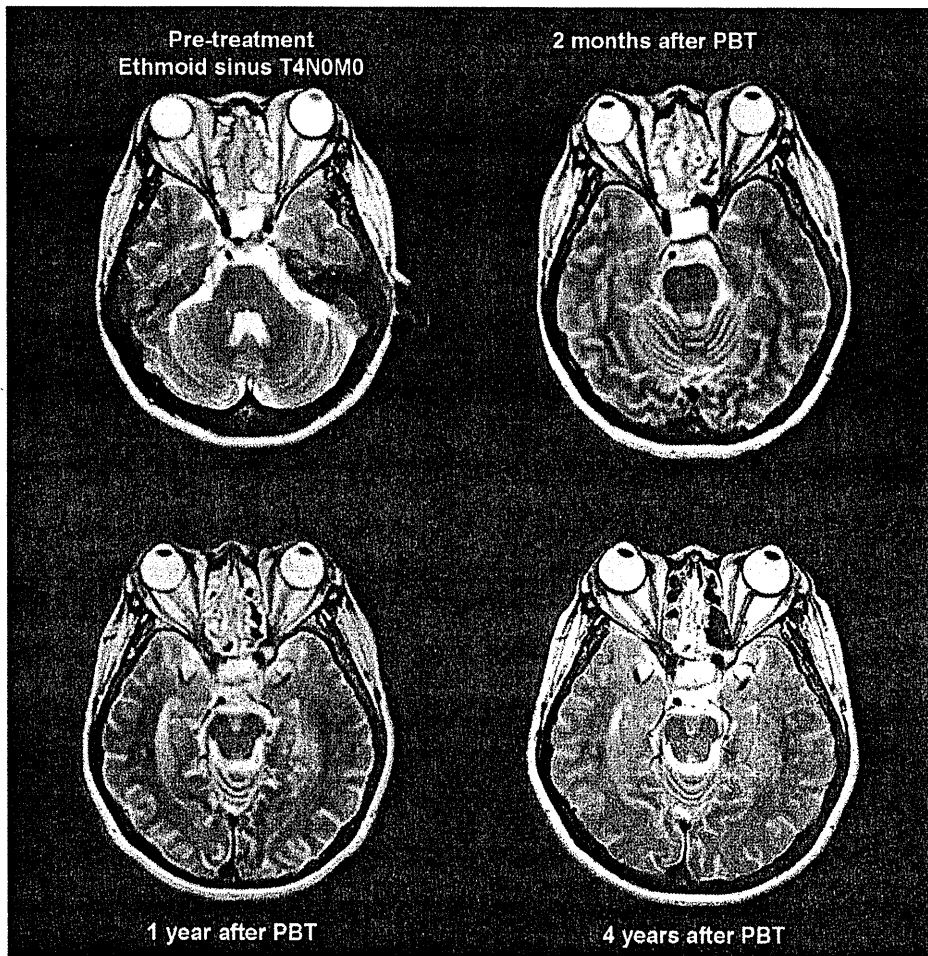
Fig. 3. Difficulty of response evaluation of proton beam therapy (PBT). The disease was undifferentiated carcinoma of the ethmoid sinus. Response evaluation at 2 months and 1 year after PBT was SD by the RECIST criteria; however, the patient has remained alive for more than 4 years without disease progression.

study had T4 disease and good performance status, which might in turn explain why no prognostic factor was found.

With regard to late toxicity, conventional radiotherapy is associated with a number of potentially severe complications, leading to radiation-induced injuries to the visual pathways, central nervous system, and adjacent bone structures. The incidence of radiation-induced unilateral or bilateral blindness has been reported to be as high as 10% to 30% (13–16). With the recent widespread adoption of intensity-modulated radiation therapy (IMRT), several studies have reported improvements in rates of severe toxicity (10, 17, 18), albeit without any improvement in efficacy. Previous studies on craniofacial surgery (6, 19), for example, have reported rates of severe complication of approximately 10% to 15%.

Consistent with this, Grade 3 to 5 late toxicities in the present series were seen in 5 patients (12.8%), and one

treatment-related death cause by CSF leakage was identified. Considering that all patients had unresectable and very advanced disease, this safety profile appears acceptable. Although advances in treatment plans for PBT have led to lower doses to critical organs and decreased late toxicity (20, 21), further reductions in toxicity remain possible.

As part of ongoing physics evaluations, our group is presently conducting further recalculations of treatment plans for patients with fatal late toxicity using Monte Carlo methods.

CONCLUSION

Our findings suggest that the clinical profile of PBT for unresectable malignancies of the nasal cavity and paranasal sinuses is sufficient to establish it as promising treatment option. Further investigation to reduce late toxicity is warranted.

REFERENCES

1. Ketcham AS, Wilkins RH, Vanburen JM, et al. A combined intracranial facial approach to the paranasal sinuses. Am J Surg 1963;106:698–703.

2. Blanco AI, Chao KS, Ozyigit G, et al. Carcinoma of paranasal sinuses: Long-term outcomes with radiotherapy. Int J Radiat Oncol Biol Phys 2004;59:51–58.

3. Hoppe BS, Stegman LD, Zelefsky MJ, et al. Treatment of nasal cavity and paranasal sinus cancer with modern radiotherapy techniques in the postoperative setting—the MSKCC experience. Int J Radiat Oncol Biol Phys 2007;67:691–702.

4. Jansen EP, Keus RB, Hilgers FJ, et al. Does the combination of radiotherapy and debulking surgery favor survival in paranasal sinus carcinoma? Int J Radiat Oncol Biol Phys 2000;48:27–35.

5. Dulguerov P, Jacobsen MS, Allal AS, et al. Nasal and paranasal sinus carcinoma: Are we making progress? A series of 220 patients and a systematic review. Cancer 2001;92:3012–3029.

6. Patel SG, Singh B, Polluri A, et al. Craniofacial surgery for malignant skull base tumors: Report of an international collaborative study. Cancer 2003;98:1179–1187.

7. Ganly I, Patel SG, Singh B, et al. Complications of craniofacial resection for malignant tumors of the skull base: Report of an international collaborative study. Head Neck 2005;27:445–451.

8. Snyers A, Janssens GO, Twickler MB, et al. Malignant tumors of the nasal cavity and paranasal sinuses: Long-term outcome and morbidity with emphasis on hypothalamic-pituitary deficiency. Int J Radiat Oncol Biol Phys 2009;73:1343–1351.

9. Dirix P, Nuyts S, Geussens Y, et al. Malignancies of the nasal cavity and paranasal sinuses: Long-term outcome with conventional or three-dimensional conformal radiotherapy. Int J Radiat Oncol Biol Phys 2007;69:1042–1050.

10. Hoppe BS, Nelson CJ, Gomez DR, et al. Unresectable carcinoma of the paranasal sinuses: Outcomes and toxicities. Int J Radiat Oncol Biol Phys 2008;72:763–769.

11. Urie MF, Sisterson JM, Koehler AM, et al. Proton beam penumbra: Effects of separation between patient and beam modifying devices. Med Phys 1986;13:734–741.

12. Ando K, Furusawa Y, Suzuki M, et al. Relative biological effectiveness of the 235 MeV proton beams at the National Cancer Center Hospital East. J Radiat Res 2001;42:79–89.

13. Martel MK, Sandler HM, Cornblath WT, et al. Dose-volume complication analysis for visual pathway structures of patients with advanced paranasal sinus tumors. Int J Radiat Oncol Biol Phys 1997;38:273–284.

14. Takeda A, Shigematsu N, Suzuki S, et al. Late retinal complications of radiation therapy for nasal and paranasal malignancies: Relationship between irradiated-dose area and severity. Int J Radiat Oncol Biol Phys 1999;44:599–605.

15. Katz TS, Mendenhall WM, Morris CG, et al. Malignant tumors of the nasal cavity and paranasal sinuses. Head Neck 2002;24:821–829.

16. Jiang GL, Tucker SL, Guttenberger R, et al. Radiation-induced injury to the visual pathway. Radiother Oncol 1994;30:17–25.

17. Daly ME, Chen AM, Bucci MK, et al. Intensity-modulated radiation therapy for malignancies of the nasal cavity and paranasal sinuses. Int J Radiat Oncol Biol Phys 2007;67:151–157.

18. Claus F, De Gersem W, De Wagter C, et al. An implementation strategy for IMRT of ethmoid sinus cancer with bilateral sparing of the optic pathways. Int J Radiat Oncol Biol Phys 2001;51:318–331.

19. Gil Z, Patel SG, Singh B, et al. Analysis of prognostic factors in 146 patients with anterior skull base sarcoma: An international collaborative study. Cancer 2007;110:1033–1941.

20. Mock U, Georg D, Bogner J, et al. Treatment planning comparison of conventional, 3D conformal, and intensity-modulated photon (IMRT) and proton therapy for paranasal sinus carcinoma. Int J Radiat Oncol Biol Phys 2004;58:147–154.

21. Lomax AJ, Goitein M, Adams J. Intensity modulation in radiotherapy: Photons versus protons in the paranasal sinus. Radiother Oncol 2003;66:11–18.

A feasibility study of a molecular-based patient setup verification method using a parallel-plane PET system

View the table of contents for this issue, or go to the journal homepage for more

A feasibility study of a molecular-based patient setup verification method using a parallel-plane PET system

Satoshi Yamaguchi[1], Masayori Ishikawa[1], Gerard Bengua[2], Kenneth Sutherland[1], Teiji Nishio[3], Satoshi Tanabe[1], Naoki Miyamoto[1], Ryusuke Suzuki[2] and Hiroki Shirato[4]

[1] Department of Medical Physics and Engineering, Hokkaido University Graduate School of Medicine, N-15 W-7 Kita-ku Sapporo 060-8638, Japan
[2] Department of Medical Physics, Hokkaido University Hospital, N-14 W-5 Kita-ku Sapporo 060-8648, Japan
[3] Particle Therapy Division, Research Center for Innovative Oncology, National Cancer Center, Kashiwa, 6-5-1 Kashiwano-ha, Kashiwa-shi, Chiba 277-8577, Japan
[4] Department of Radiology, Hokkaido University Graduate School of Medicine, N-15 W-7 Kita-ku Sapporo, 060-8638 Japan

E-mail: masayori@med.hokudai.ac.jp

Abstract
A feasibility study of a novel PET-based molecular image guided radiation therapy (m-IGRT) system was conducted by comparing PET-based digitally reconstructed planar image (PDRI) registration with radiographic registration. We selected a pair of opposing parallel-plane PET systems for the practical implementation of this system. Planar images along the in-plane and cross-plane directions were reconstructed from the parallel-plane PET data. The in-plane and cross-plane FWHM of the profile of 2 mm diameter sources was approximately 1.8 and 8.1 mm, respectively. Therefore, only the reconstructed in-plane image from the parallel-plane PET data was used in the PDRI registration. In the image registration, five different sizes of ^{18}F cylindrical sources (diameter: 8, 12, 16, 24, 32 mm) were used to determine setup errors. The data acquisition times were 1, 3 and 5 min. Image registration was performed by five observers to determine the setup errors from PDRI registration and radiographic registration. The majority of the mean registration errors obtained from the PDRI registration were not significantly different from those obtained from the radiographic registration. Acquisition time did not appear to result in significant differences in the mean registration error. The mean registration error for the PDRI registration was found to be 0.93 ± 0.33 mm. This is not statistically different from the radiographic registration which had a mean registration error of 0.92 ± 0.27 mm. Our results suggest